The Astrophysical Journal, 761:73 (12pp), 2012 December 10 doi:10.1088/0004-637X/761/1/73

X-RAY PROPERTIES OF INTERMEDIATE-MASS BLACK HOLES IN ACTIVE GALAXIES. III. SPECTRAL ENERGY DISTRIBUTION AND POSSIBLE EVIDENCE FOR INTRINSICALLY X-RAY-WEAK ACTIVE GALACTIC NUCLEI

Ruobing Dong(董若冰)[1], Jenny E. Greene[1], and Luis C. Ho[2]
[1] Department of Astrophysical Sciences, Princeton University, Princeton, NJ 08544, USA; rdong@princeton.edu, jgreene@princeton.edu
[2] The Observatories of the Carnegie Institution for Science, 813 Santa Barbara St., Pasadena, CA 91101, USA; lho@obs.carnegiescience.edu
Received 2012 September 8; accepted 2012 October 23; published 2012 November 27

ABSTRACT

We present a systematic X-ray study, the third in a series, of 49 active galactic nuclei with intermediate-mass black holes (IMBH; $\sim 10^5$–$10^6\ M_\odot$) using *Chandra* observations. We detect 42 out of 49 targets with a 0.5–2 keV X-ray luminosity 10^{41}–10^{43} erg s^{-1}. We perform spectral fitting for the 10 objects with enough counts (>200), and they are all well fit by a simple power-law model modified by Galactic absorption, with no sign of significant intrinsic absorption. While we cannot fit the X-ray spectral slope directly for the rest of the sample, we estimate it from the hardness ratio and find a range of photon indices consistent with those seen in more luminous and massive objects. The X-ray-to-optical spectral slope (α_{ox}) of our IMBH sample is systematically flatter than in active galaxies with more massive black holes, consistent with the well-known correlation between α_{ox} and UV luminosity. Thanks to the wide dynamic range of our sample, we find evidence that α_{ox} increases with decreasing M_{BH} as expected from accretion disk models, where the UV emission systematically decreases as M_{BH} decreases and the disk temperature increases. We also find a long tail toward low α_{ox} values. While some of these sources may be obscured, given the high L_{bol}/L_{Edd} values in the sample, we argue that some may be intrinsically X-ray-weak, perhaps owing to a rare state that radiates very little coronal emission.

Key words: galaxies: active – galaxies: nuclei – galaxies: Seyfert – galaxies: statistics – X-rays: galaxies

Online-only material: color figures

1. INTRODUCTION

Broadband spectral energy distributions (SEDs) provide rich diagnostics on the accretion process in black hole (BH) studies (e.g., Elvis et al. 1994; Ho 1999; Vasudevan et al. 2009; Trichas et al. 2012). Not only are SEDs important for measuring the total bolometric luminosity of the active galactic nucleus (AGN), for constraining models of accretion disks, and for understanding how BHs grow, they also determine the impact of a BH on its surroundings. If supermassive BHs truly play an important role in the evolution of galaxies, we must understand how fundamental properties of the AGN, such as BH mass and accretion rate, impact the SED.

The study of accretion onto stellar-mass BHs is quite mature. Stellar-mass BHs have accurate BH mass measurements derived from the orbits of their stellar companions (e.g., Cantrell et al. 2010) and because the timescales are quite short, it is possible to watch individual systems change luminosity states over many orders of magnitude, thus determining how the SED changes as a function of the mass accretion rate (e.g., Remillard & McClintock 2006; Fender et al. 2009; Straub et al. 2011). Since the accretion disks around stellar-mass BHs peak in the X-rays when the BHs are in a high state, there are also direct measurements of the peak emission from the BH. In contrast, with a small number of exceptions, we do not have reliable BH mass measurements for supermassive BHs in AGNs. Supermassive BH accretion disks peak in the far-UV, where we cannot obtain direct observations (e.g., Shields 1978). Furthermore, changes in accretion rate occur over prohibitively long timescales in general, so we can only probe a range of accretion rates by looking at large populations. Then, we are at the mercy of particular samples, and selection effects substantially complicate our efforts to disentangle the effects of M_{BH} and Eddington ratio on the observed SEDs.

Thanks to the Sloan Digital Sky Survey (SDSS; York et al. 2000), we were able to find a large sample of accreting BHs with the lowest BH masses known (10^5–$10^6\ M_\odot$). Greene & Ho (2004, hereinafter GH04) systematically searched for and found an initial sample of 19 intermediate-mass black holes (IMBHs) from the first SDSS data release (DR1). With SDSS DR4, two larger samples have been identified, by Greene & Ho (2007b; hereinafter GH07) and Dong et al. (2012). In GH07, the BH mass is inferred from the photoionized broad-line region (BLR) gas as $M_{BH} = fRv^2/G$, where R and v are the radius and velocity dispersion of the BLR gas, and f is a scaling factor that accounts for the unknown geometry of the BLR, assumed here to be spherical ($f = 0,75$; Netzer 1990). The BLR velocity dispersion is derived from the Hα line width, and the BLR radius is inferred from the AGN luminosity (Greene & Ho 2005), using the so-called radius–luminosity relation. The relation between BLR radius and luminosity is derived from reverberation mapping of AGNs, for which radii are measured based on the delay between variations in the AGN photoionizing continuum and BLR line emission (e.g., Kaspi et al. 2005; Greene & Ho 2005; Bentz et al. 2009).

BH masses derived in this way are indirect, and they rely on the radius–luminosity relation, which is susceptible to large systematic errors (due to uncertainties in the BLR geometry and kinematics; e.g., Krolik 2001). It is certainly true that on a galaxy-by-galaxy basis we may well be fooled by high-mass outliers. However, we have some confidence that the average BH masses in our sample are low. In one case, reverberation mapping points to a very low mass for a galaxy from our sample (Rafter et al. 2011). For the rest, we must rely on indirect scalings with the host galaxy properties. Overall, the host galaxies have low mass. They are typically about a magnitude below L^* (Barth et al. 2005; Greene et al. 2008; Xiao et al. 2011; Jiang

et al. 2011a) and the stellar velocity dispersions are also low (Barth et al. 2005; Xiao et al. 2011). The BH masses expected from the stellar velocity dispersion measurements are typically 10^5–10^6 $M_\odot$ for our sample (Xiao et al. 2011). Based on bulge masses, instead, the expected BH masses would be an order of magnitude or so larger (Jiang et al. 2011a, 2011b). As further caveats, we note that we have extrapolated both the M–σ and M–$M_{\rm bulge}$ correlations, and also that the M–σ relation may break down in spirals (e.g., Greene et al. 2010; Hu 2008; Kormendy & Bender 2011).

We already have some interesting constraints on the broad-band SEDs for the AGNs in the GH07 sample. We have found that the sources are very radio-quiet on average (Greene et al. 2006). We have seen very indirect evidence that the far-UV slopes are steeper than in more massive systems (Greene & Ho 2005; Ludwig et al. 2012). Finally, we saw tantalizing hints that the sources are relatively X-ray bright (Greene & Ho 2007a; Miniutti et al. 2009; Desroches et al. 2009). In this paper, we present *Chandra* observations for a larger sample of sources from GH07. The current sample contain 49 sources drawn from the 174 presented in GH07, excluding the less secure *c* sample (GH07 flagged a subset of their detections as low-significance in cases that they could not be confident in the presence of a broad Hα line from the SDSS spectrum alone). The general selection strategy is to observe the nearest galaxies, with the average redshift of the 49 objects being $\sim$0.05 comparing to $\sim$0.09 for the 174 GH07 objects. The observations are 2 ks "snapshots," which allow us to observe a large number of targets within a limited time. We will argue that our X-ray observations point to real changes in the structures of accretion disks as a function of $M_{\rm BH}$.

The structure of this paper is as follows. We present the data analysis and spectral fitting processes in Section 2, where we try various models to fit the spectra. Then, in Section 3 we discuss the X-ray properties of the sample. The broader SEDs of the sample is discussed in Section 4, specifically we focus on the ratio of optical/UV to X-rays. We identify a potential subgroup of intrinsically X-ray-weak candidates in Section 5, and discuss the possible origins of their X-ray weakness. A short summary is provided in Section 6. The cosmological parameters assumed in this paper are $H_0 = 71$ km s^{-1} Mpc^{-1}, $\Omega_m = 0.27$, and $\Omega_\Lambda = 0.75$ (Spergel et al. 2003).

2. OBSERVATIONS AND DATA ANALYSIS

The *Chandra* (Weisskopf et al. 1996) observations in this work were taken between 2009 September and 2010 September (proposal number 11700259). They are snapshot observations, with effective exposure times of $\sim$2 ks. As in Greene & Ho (2007a, Paper I) and Desroches et al. (2009, Paper II), the Advanced CCD Imaging Spectrometer (ACIS; Garmire et al. 2003) was used, and images were obtained at the aim point of the S3 CCD in faint mode. We only read out 1/8 of the chip to reduce the effects of pile-up.

The basic data reduction steps are described in Papers I and II. Here we give only a brief summary. We begin with the standard Level 2 event files processed by the Chandra X-Ray Center, which already have been corrected for cosmic rays filtered for good time intervals. Events below 0.3 keV and above 8 keV are rejected in the analysis to avoid calibration uncertainties at low energies and to limit background contamination at high energies (Gallo et al. 2008). We follow the standard procedure of detecting faint point sources in *Chandra* observations, and we use the task `celldetect` in the Chandra Interactive Analysis of Observations (CIAO) package[3] with default parameters to detect sources and extract their centroid positions. We set an initial detection threshold of signal-to-noise ratio (S/N) $\geqslant 3$. In every case `celldetect` yields 0 or 1 detection, with a detection being a point source at the aim point. We detected 42 out of 49 sources. All but two were detected with an S/N $\geqslant 3$, while the final two had $3 >$ S/N $\geqslant 2$. A detection threshold of S/N $\geqslant 3$ is the standard value in *Chandra* faint source observations, as recommended in CIAO. However, we note that in the regime of nearly zero background, a low-S/N detection such as S/N = 2 can still be a statistically significant detection. Studies of simulated *Chandra* data[4] show that the false detection rate with S/N $\geqslant 1$ in 10 ks ACIS on-axis observations is about 0.1 per four imaging chips in ACIS-I. The false detection rate of S/N $\geqslant 2$ in our 2 ks observations should be even lower. Interestingly, we note that the detection rate for this sample with 2 ks snapshots (42/49) is actually higher than that in the GH04 sample with 5 ks observations (13/18; Paper II). This apparent peculiarity is presumably due to the smaller distances of the current sample, whose average redshift is $\sim$0.05, compared with $\sim$0.09 for the GH04 sample. The position difference between *Chandra* and SDSS is less than 1″ for all sources, and less than 0.″5 for 90% of the sample, which is the spatial resolution of *Chandra*.

The on-axis point-spread function of *Chandra* contains 95% of the encircled energy within 1″. We therefore extract counts from a 2″ radius circle centered on the source, in the soft (0.5–2 keV; C_s) and hard (2–8 keV; C_h) bands. We measure background rates from a concentric annulus with inner radius 7″ and outer radius 15″, and background-corrected count rates are calculated using the CIAO task `dmextract`. The background rates within the aperture are always very low ($<$1 count s^{-1} for all cases). For the undetected objects, we calculate an upper limit of the counts in the full band necessary to make a theoretical detection with an S/N of 2 using our source detection procedure. We follow the CIAO help page[5] on how to determine the S/N given the source and background counts, then divide this full-band count upper limit into C_s and C_h, assuming a photon spectral index $\Gamma = 2$ [$N(E) \propto E^{-\Gamma}$], which is the average value from Papers I and II and from the current sample (see below). We note here that this procedure is different from that used in Paper II, where the C_s and C_h upper limits for non-detections were calculated to have a theoretical detection with an S/N of 2 in each band separately, given the background counts in each band. The current strategy is more accurate in the sense that it is a direct analog to the detected cases, while the previous strategy yielded an unrealistically high upper limit. When they are used in the analysis below, the undetected objects from Paper II are reprocessed following the new strategy.

2.1. Hardness Ratios

As in Gallagher et al. (2005) and in Papers I and II, we measure the hardness ratio, HR $\equiv (C_h - C_s)/(C_h + C_s)$, for all the detected targets. This gives a crude estimate of the spectral shape, from which we can then infer a spectral index $\Gamma_{\rm HR}$. We use the CIAO task `psextract`[6] to get the instrumental response functions, both the auxiliary response file (ARF) and the redistribution matrix file (RMF). We use the spectral-fitting

[3] http://cxc.harvard.edu/ciao/download/doc/detect_manual/cell_theory.html

[4] http://cxc.harvard.edu/ciao/download/doc/detect_manual/cell_false.html

[5] http://cxc.harvard.edu/ciao/download/doc/detect_manual/cell_theory.html

[6] Since we use −120° ACIS data taken in FAINT mode, which have gone through Reprocessing III, we run `mkacisrmf` after `psextract` as recommended by the CIAO team (http://cxc.harvard.edu/ciao/why/mkacisrmf.html), and we rerun `mkarf` after that to match the energy grids for the ARF and RMF files.

package XSPEC (Arnaud 1996) to generate artificial spectra with known spectral slopes ($0 < \Gamma < 4$) and Galactic absorption (Dickey & Lockman 1990; Table 1). Then we "observe" the artificial spectra using the ARF and RMF extracted for each observation, and measure the HR for each input Γ. By comparing each observed HR with the HR from artificial spectra, we infer $\Gamma_{\rm HR}$, as listed in Table 1. Below we check the validity of this method by comparing $\Gamma_{\rm HR}$ with $\Gamma_{\rm fit}$ from actual spectral fitting of bright sources, and the comparison shows that the HR-based spectral indices are reasonable (but see the caveat in Section 3.2). For the sake of uniformity, all the analysis in this paper, unless specified otherwise, is done using $\Gamma_{\rm HR}$.

2.2. Spectral Fitting

We perform spectral fitting for the 10 sources with sufficient total counts (>200 in the entire band). We bin the event files to achieve at least 20 counts per bin to ensure the validity of χ^2 statistics. We use the task `psextract` to extract the spectra, using the same aperture and background region as above, and the appropriate RMF and ARF files. For most sources we limit the energy range to ~0.3–5 keV to avoid large uncertainties due to detector response and low counts, while for some of the faintest ones we reduce this range even further (see Table 1).

All of the spectra are fitted with XSPEC with a single absorbed power-law (PL) model, with absorption fixed to the Galactic value (Dickey & Lockman 1990). We list the fitted parameters as well as the χ^2 statistics in Table 2 and provide the spectra and their fits in Figure 1. The quoted errors are at the 90% confidence level. With the reduced χ^2_ν being consistent with 1 and the fitting residuals randomly distributed, a simple absorbed PL model proves to be adequate for all the sources, with no additional components needed. To check whether there is any sign of intrinsic absorption, we fit the spectrum with a PL model modified by an absorption component in addition to the fixed Galactic component. The results are generally worse than the simple Galactic absorbed PL model, as indicated by their χ^2_ν being farther from 1. There is no evidence for intrinsic absorption in any of the sources, at the 90% confidence level; this is consistent with the conclusions from Papers I and II. We note that this result might be influenced by the low source counts and limited spectral coverage of our snapshot observations.

We also try to look for possible evidence for a soft excess in the spectra. Soft excesses above a fiducial PL are widely observed in luminous AGNs. It is modeled in various ways, such as a broken PL, a multicolor disk blackbody (diskbb), or a Comptonized multicolor disk (Wang et al. 2004; Miniutti et al. 2009), although its origin is still hotly debated (Crummy et al. 2006; Done & Nayakshin 2007; Miniutti et al. 2009). We fit the spectra using a Galactic absorbed PL+diskbb model to see if there is any evidence for a soft excess component in our sample. In general, this model does not provide an obviously better fit to the spectra. Most of the values for the fitted inner disk temperature are unnaturally high, with $T_{\rm in} \approx 1.5$ keV), to be compared with typical values of $T_{\rm in} \approx 0.15$ keV seen in narrow-line Seyfert 1 (NLS1) galaxies (Leighly 1999) and in the GH04 objects bright enough to be studied with *XMM-Newton* (Miniutti et al. 2009).

Another way to look for the soft excess is to fit the hard-band spectrum using a single absorbed PL, and then extrapolate it into the soft band to see whether there is any additional excess above the PL (Paper I; Miniutti et al. 2009). Unfortunately, we can only do this for two sources, SDSS J0903+0457 and SDSS J1559+3501, which have enough counts in the hard band to ensure a reliable fit. Following Paper I, we fit the data using only photons with energies above 1.5 keV with a PL component modified by fixed Galactic absorption. In the case of SDSS J1559+3501, there is no excess when the PL is extrapolated to the soft band. In fact, the fitted parameters agree, within the errors, with the fit to the full-band spectrum (0.3–5 keV), indicating that the entire spectrum is reasonably described by a single absorbed PL model; adding an extra diskbb component is not necessary. However, in the case of SDSS J0903+0457, as shown in the left panel of Figure 2, a soft excess clearly stands out when we fix the power-law component using only photons with energies above 1.5 keV. The hard-band $\Gamma_h = 1.99 \pm 0.20$ is significantly flatter than that obtained from fitting the full spectrum, $\Gamma_{\rm fit} = 2.42 \pm 0.06$. Adding a diskbb component in addition to the PL to model the full spectrum (0.3–5 keV) gives a significant improvement to the fit (right panel of Figure 2), resulting in $\chi^2_\nu = 61.7/50$ (the power-law component is fixed from fitting photons with energies above 1.5 keV) over the previous value of $\chi^2_\nu = 83.3/50$. The inner disk temperature of $T_{\rm in} = 0.15 \pm 0.006$ keV is consistent with values seen in other IMBHs (Miniutti et al. 2009; Thornton et al. 2009). We conclude that for this object, a two component model (pl+diskbb) is consistent with the data, while there is no clear evidence for a soft excess in the rest of the sample.

However, an additional diskbb component has been firmly detected by Miniutti et al. (2009) for at least three out of four IMBH AGNs selected from the GH04 sample, and Thornton et al. (2009) show that POX 52 also contains a prominent soft component. Moreover, using the same technique, Porquet et al. (2004) found that soft excesses are very common in their sample of higher mass ($10^7\,M_\odot < M_{\rm BH} < 10^9\,M_\odot$) but also high-Eddington ratio ($L_{\rm bol}/L_{\rm Edd} = L_{\rm bol}/L_{\rm Edd} \approx 0.1$–1) AGNs. Thus, we again caution that the non-detection of a soft component in most of our objects may be an artifact of the low source counts and narrow energy coverage of our snapshot observations. Indeed, none of the objects for which Miniutti et al. (2009) detected a soft excess in *XMM-Newton* observations show evidence for such a component in their shallower *Chandra* observations.

The "HR comparison" method for estimating the X-ray spectral index, $\Gamma_{\rm HR}$, when spectral fitting is not applicable due to low source counts, has been used in the literature before (e.g., Gallagher et al. 2005; Papers I and II) and is potentially a very useful method in observations aiming at distant, faint sources. Here we verify the reliability of this method, by combining data from Papers I and II and the current work when both spectral fitting and HR comparison are available. Figure 3 shows the result, where error bars indicate the 90% confidence level for the spectral fitting $\Gamma_{\rm fit}$ and the uncertainties propagated from HR to $\Gamma_{\rm HR}$. The two Γ measurements generally agree well, especially at the steep end, with an average difference of 0.04 and a standard deviation of 0.18.

3. X-RAY PROPERTIES

Compared with most AGNs previous studied, our optically selected sample[7] is distinguished by two unique features: low

[7] Unless otherwise specified, the discussion below refers to the observations reported in this paper plus those from GH04 (published in Papers I and II) that remain in the GH07 sample. A few of the original GH04 objects no longer satisfy the mass cut of GH07, according to the updated mass estimator in GH07. The final combined sample contains 61 sources, 49 from this study and 12 from Papers I and II. In addition to the revised X-ray upper limits described in Section 2, all the optical parameters used in the present analysis have also been updated with the most recent values from GH07.

Table 1
X-Ray Properties

SDSS ID	D_L (Mpc)	$\log N_{\rm H}$ ($\rm cm^{-2}$)	S/N	C_s (count $\rm s^{-1}$)	C_h (count $\rm s^{-1}$)	$\Gamma_{\rm HR}$	$\log f_s$ (erg $\rm s^{-1}$ $\rm cm^{-2}$)	$\log f_h$ (erg $\rm s^{-1}$ $\rm cm^{-2}$)	$\log L_s$ (erg $\rm s^{-1}$)	$\log L_h$ (erg $\rm s^{-1}$)	$\alpha_{\rm ox}$
(1)	(2)	(3)	(4)	(5)	(6)	(7)	(8)	(9)	(10)	(11)	(12)
J0001−1002	215	20.48	3.7	0.0061 ± 0.0018	0.0045 ± 0.0015	1.29 ± 0.33	$-13.60^{+0.12}_{-0.15}$	$-13.05^{+0.16}_{-0.22}$	$41.15^{+0.12}_{-0.15}$	$41.70^{+0.16}_{-0.22}$	−1.37
J0228−0902	322	20.55	7.4	0.0280 ± 0.0039	0.0060 ± 0.0018	2.22 ± 0.27	$-12.91^{+0.07}_{-0.07}$	$-13.02^{+0.14}_{-0.18}$	$42.19^{+0.07}_{-0.07}$	$42.08^{+0.14}_{-0.18}$	−1.13
J0304+0028	194	20.86	25.5	0.2599 ± 0.0115	0.0788 ± 0.0063	2.07 ± 0.07	$-11.90^{+0.02}_{-0.02}$	$-11.89^{+0.04}_{-0.04}$	$42.76^{+0.02}_{-0.02}$	$42.77^{+0.04}_{-0.04}$	−1.20
J0731+3926	212	20.79	18.7	0.1813 ± 0.0104	0.0285 ± 0.0041	2.54 ± 0.12	$-12.05^{+0.03}_{-0.03}$	$-12.37^{+0.07}_{-0.08}$	$42.68^{+0.03}_{-0.03}$	$42.36^{+0.07}_{-0.08}$	−1.07
J0806+2420	182	20.61	6.6	0.0191 ± 0.0031	0.0076 ± 0.0020	1.78 ± 0.22	$-13.08^{+0.07}_{-0.08}$	$-12.88^{+0.12}_{-0.15}$	$41.52^{+0.07}_{-0.08}$	$41.72^{+0.12}_{-0.15}$	−1.43
J0809+4416	238	20.70	11.6	0.0569 ± 0.0054	0.0173 ± 0.0030	2.01 ± 0.15	$-12.59^{+0.04}_{-0.05}$	$-12.54^{+0.08}_{-0.10}$	$42.25^{+0.04}_{-0.05}$	$42.30^{+0.08}_{-0.10}$	−1.20
J0816+2506	324	20.59	5.5	0.0151 ± 0.0029	0.0070 ± 0.0020	1.66 ± 0.26	$-13.19^{+0.08}_{-0.10}$	$-12.90^{+0.14}_{-0.17}$	$41.92^{+0.08}_{-0.10}$	$42.21^{+0.14}_{-0.17}$	−1.27
J0824+2959	109	20.58	6.8	0.0126 ± 0.0025	0.0166 ± 0.0029	0.88 ± 0.20	$-13.28^{+0.08}_{-0.10}$	$-12.43^{+0.09}_{-0.11}$	$40.88^{+0.08}_{-0.10}$	$41.73^{+0.09}_{-0.11}$	−1.60
J0852+5228	286	20.40	7.7	0.0250 ± 0.0036	0.0097 ± 0.0022	1.76 ± 0.20	$-12.98^{+0.06}_{-0.07}$	$-12.77^{+0.11}_{-0.14}$	$42.01^{+0.06}_{-0.07}$	$42.23^{+0.11}_{-0.14}$	−1.35
J0903+0457	250	20.62	36.9	0.5916 ± 0.0179	0.1003 ± 0.0074	2.42 ± 0.06	$-11.57^{+0.02}_{-0.02}$	$-11.82^{+0.04}_{-0.04}$	$43.31^{+0.02}_{-0.02}$	$43.06^{+0.04}_{-0.04}$	−1.03
J0924+5607	107	20.42	6.4	0.0160 ± 0.0029	0.0103 ± 0.0023	1.38 ± 0.21	$-13.18^{+0.08}_{-0.09}$	$-12.70^{+0.11}_{-0.13}$	$40.96^{+0.08}_{-0.09}$	$41.44^{+0.11}_{-0.13}$	−1.61
J0933+5347	251	20.23	11.6	0.0600 ± 0.0055	0.0080 ± 0.0020	2.51 ± 0.19	$-12.59^{+0.04}_{-0.05}$	$-12.92^{+0.11}_{-0.14}$	$42.29^{+0.04}_{-0.05}$	$41.96^{+0.11}_{-0.14}$	−1.37
J0941+0324	268	20.58	19.0	0.1517 ± 0.0088	0.0296 ± 0.0039	2.30 ± 0.11	$-12.17^{+0.03}_{-0.03}$	$-12.33^{+0.06}_{-0.07}$	$42.77^{+0.03}_{-0.03}$	$42.60^{+0.06}_{-0.07}$	−1.20
J0953+5627	294	20.04	...	<0.0031	<0.0008	...	<−13.90	<−13.90	<41.12	<41.12	<−1.63
J0954+4032	299	20.19	9.4	0.0369 ± 0.0045	0.0152 ± 0.0029	1.68 ± 0.17	$-12.82^{+0.05}_{-0.06}$	$-12.56^{+0.09}_{-0.11}$	$42.21^{+0.05}_{-0.06}$	$42.47^{+0.09}_{-0.11}$	−1.37
J1035+0734	299	20.46	7.3	0.0244 ± 0.0035	0.0096 ± 0.0022	1.75 ± 0.19	$-12.99^{+0.06}_{-0.07}$	$-12.77^{+0.11}_{-0.13}$	$42.04^{+0.06}_{-0.07}$	$42.26^{+0.11}_{-0.13}$	−1.35
J1058+4825	327	20.09	...	<0.0031	<0.0008	...	<−13.90	<−13.90	<41.21	<41.21	<−1.61
J1105+5941	146	19.76	13.6	0.0729 ± 0.0063	0.0351 ± 0.0044	1.54 ± 0.11	$-12.54^{+0.04}_{-0.04}$	$-12.19^{+0.05}_{-0.06}$	$41.87^{+0.04}_{-0.04}$	$42.23^{+0.05}_{-0.06}$	−1.40
J1125+0220	213	20.58	9.5	0.0450 ± 0.0050	0.0115 ± 0.0025	2.10 ± 0.18	$-12.70^{+0.05}_{-0.06}$	$-12.73^{+0.10}_{-0.12}$	$42.04^{+0.05}_{-0.06}$	$42.01^{+0.10}_{-0.12}$	−1.37
J1136+4246	317	20.34	12.2	0.0601 ± 0.0055	0.0202 ± 0.0032	1.85 ± 0.14	$-12.60^{+0.04}_{-0.04}$	$-12.46^{+0.08}_{-0.09}$	$42.48^{+0.04}_{-0.04}$	$42.62^{+0.08}_{-0.09}$	−1.14
J1137+4113	319	20.32	10.5	0.0518 ± 0.0052	0.0104 ± 0.0023	2.23 ± 0.17	$-12.66^{+0.05}_{-0.05}$	$-12.79^{+0.10}_{-0.13}$	$42.43^{+0.05}_{-0.05}$	$42.30^{+0.10}_{-0.13}$	−1.21
J1143+5500	117	20.03	...	<0.0033	<0.0008	...	<−13.88	<−13.88	<40.35	<40.35	<−1.85
J1153+4612	104	20.30	26.7	0.2829 ± 0.0119	0.0715 ± 0.0060	2.05 ± 0.07	$-11.93^{+0.02}_{-0.02}$	$-11.93^{+0.04}_{-0.05}$	$42.19^{+0.02}_{-0.02}$	$42.19^{+0.04}_{-0.05}$	−1.33
J1215+0148	317	20.27	6.5	0.0210 ± 0.0033	0.0056 ± 0.0017	2.01 ± 0.25	$-13.06^{+0.07}_{-0.08}$	$-13.03^{+0.14}_{-0.18}$	$42.02^{+0.07}_{-0.08}$	$42.05^{+0.14}_{-0.18}$	−1.38
J1223+5814	61	20.09	19.5	0.1541 ± 0.0092	0.0642 ± 0.0059	1.67 ± 0.08	$-12.21^{+0.03}_{-0.03}$	$-11.94^{+0.05}_{-0.05}$	$41.45^{+0.03}_{-0.03}$	$41.72^{+0.05}_{-0.05}$	−1.30
J1227+6306	350	20.27	4.4	0.0126 ± 0.0026	0.0027 ± 0.0012	2.17 ± 0.38	$-13.28^{+0.09}_{-0.11}$	$-13.36^{+0.20}_{-0.30}$	$41.89^{+0.09}_{-0.11}$	$41.81^{+0.20}_{-0.30}$	−1.34
J1254+4628	272	20.15	2.9	0.0071 ± 0.0020	0.0005 ± 0.0005	2.97 ± 0.86	∼−13.51	∼−14.17	∼41.44	∼40.78	−1.43
J1308+5052	239	20.07	15.2	0.0950 ± 0.0069	0.0303 ± 0.0039	1.86 ± 0.11	$-12.41^{+0.03}_{-0.03}$	$-12.28^{+0.06}_{-0.07}$	$42.42^{+0.03}_{-0.03}$	$42.55^{+0.06}_{-0.07}$	−1.17
J1313+0519	214	20.34	15.9	0.1159 ± 0.0076	0.0156 ± 0.0028	2.52 ± 0.14	$-12.30^{+0.03}_{-0.03}$	$-12.63^{+0.08}_{-0.10}$	$42.44^{+0.03}_{-0.03}$	$42.11^{+0.08}_{-0.10}$	−1.17
J1317+0556	243	20.36	4.8	0.0076 ± 0.0020	0.0091 ± 0.0022	0.92 ± 0.26	$-13.51^{+0.10}_{-0.13}$	$-12.70^{+0.12}_{-0.15}$	$41.34^{+0.10}_{-0.13}$	$42.15^{+0.12}_{-0.15}$	−1.54
J1319+1056	286	20.27	...	<0.0033	<0.0008	...	<−13.86	<−13.86	<41.13	<41.13	<−1.76
J1322+4226	332	20.09	5.3	0.0112 ± 0.0024	0.0071 ± 0.0019	1.36 ± 0.25	$-13.35^{+0.09}_{-0.11}$	$-12.86^{+0.13}_{-0.16}$	$41.77^{+0.09}_{-0.11}$	$42.27^{+0.13}_{-0.16}$	−1.39
J1347+4743	285	20.23	11.5	0.0697 ± 0.0062	0.0099 ± 0.0023	2.47 ± 0.19	$-12.53^{+0.04}_{-0.05}$	$-12.83^{+0.11}_{-0.13}$	$42.46^{+0.04}_{-0.05}$	$42.16^{+0.11}_{-0.13}$	−1.33
J1433+5258	208	20.15	2.6	0.0022 ± 0.0011	0.0043 ± 0.0015	0.53 ± 0.45	$-14.07^{+0.18}_{-0.30}$	$-12.97^{+0.19}_{-0.25}$	$40.65^{+0.18}_{-0.30}$	$41.74^{+0.19}_{-0.25}$	−1.59
J1441−0235	194	20.64	...	<0.0034	<0.0009	...	<−13.83	<−13.83	<40.83	<40.83	<−1.88
J1534+0408	172	20.63	8.3	0.0352 ± 0.0044	0.0049 ± 0.0016	2.57 ± 0.27	$-12.79^{+0.06}_{-0.07}$	$-13.14^{+0.15}_{-0.20}$	$41.77^{+0.06}_{-0.07}$	$41.41^{+0.15}_{-0.20}$	−1.22
J1537+3122	248	20.37	...	<0.0034	<0.0008	...	<−13.85	<−13.85	<41.02	<41.02	<−1.76
J1542+3100	304	20.38	16.1	0.1130 ± 0.0077	0.0228 ± 0.0034	2.23 ± 0.12	$-12.32^{+0.03}_{-0.03}$	$-12.44^{+0.07}_{-0.08}$	$42.73^{+0.03}_{-0.03}$	$42.61^{+0.07}_{-0.08}$	−1.14
J1543+0307	291	20.75	9.8	0.0379 ± 0.0044	0.0140 ± 0.0027	1.88 ± 0.17	$-12.76^{+0.05}_{-0.06}$	$-12.62^{+0.09}_{-0.11}$	$42.25^{+0.05}_{-0.06}$	$42.39^{+0.09}_{-0.11}$	−1.35
J1559+3501	134	20.32	40.4	0.6521 ± 0.0183	0.1502 ± 0.0088	2.13 ± 0.05	$-11.56^{+0.01}_{-0.01}$	$-11.61^{+0.03}_{-0.03}$	$42.78^{+0.01}_{-0.01}$	$42.72^{+0.03}_{-0.03}$	−1.27
J1618−0020	252	20.85	6.9	0.0254 ± 0.0036	0.0061 ± 0.0018	2.25 ± 0.24	$-12.91^{+0.07}_{-0.08}$	$-13.02^{+0.13}_{-0.17}$	$41.98^{+0.07}_{-0.08}$	$41.87^{+0.13}_{-0.17}$	−1.23
J1624−0054	204	20.87	5.5	0.0164 ± 0.0029	0.0046 ± 0.0015	2.14 ± 0.28	$-13.10^{+0.08}_{-0.10}$	$-13.12^{+0.15}_{-0.20}$	$41.60^{+0.08}_{-0.10}$	$41.57^{+0.15}_{-0.20}$	−1.41
J1626+3502	148	20.16	5.1	0.0123 ± 0.0025	0.0061 ± 0.0018	1.55 ± 0.02	$-13.30^{+0.08}_{-0.10}$	$-12.94^{+0.11}_{-0.15}$	$41.12^{+0.08}_{-0.10}$	$41.48^{+0.11}_{-0.15}$	−1.55
J1632−0028	189	20.58	5.1	0.0123 ± 0.0025	0.0041 ± 0.0015	1.91 ± 0.30	$-13.27^{+0.09}_{-0.11}$	$-13.15^{+0.16}_{-0.22}$	$41.37^{+0.09}_{-0.11}$	$41.48^{+0.16}_{-0.22}$	−1.51
J1632+2437	314	20.79	...	<0.0032	<0.0009	...	<−13.83	<−13.83	<41.24	<41.24	<−1.59
J1656+3714	277	20.26	5.1	0.0141 ± 0.0027	0.0035 ± 0.0013	2.06 ± 0.32	$-13.23^{+0.08}_{-0.10}$	$-13.24^{+0.17}_{-0.24}$	$41.74^{+0.08}_{-0.10}$	$41.73^{+0.17}_{-0.24}$	−1.53
J2058−0650	329	20.70	10.7	0.0553 ± 0.0055	0.0142 ± 0.0028	2.13 ± 0.16	$-12.60^{+0.05}_{-0.05}$	$-12.64^{+0.09}_{-0.11}$	$42.52^{+0.05}_{-0.05}$	$42.48^{+0.09}_{-0.11}$	−1.32
J2348−0912	348	20.45	2.6	0.0022 ± 0.0011	0.0043 ± 0.0015	0.56 ± 0.44	$-14.06^{+0.18}_{-0.30}$	$-12.98^{+0.19}_{-0.24}$	$41.11^{+0.18}_{-0.30}$	$42.19^{+0.19}_{-0.24}$	−1.56
J2358+0035	338	20.51	7.8	0.0312 ± 0.0040	0.0036 ± 0.0014	2.68 ± 0.30	$-12.85^{+0.06}_{-0.07}$	$-13.29^{+0.17}_{-0.23}$	$42.29^{+0.06}_{-0.07}$	$41.85^{+0.17}_{-0.23}$	−1.21

Notes. Column (1) Abbreviated SDSS name. Column (2) Luminosity distance, calculated using the observed SDSS redshift and our adopted cosmology. Column (3) Column density of neutral hydrogen, from Dickey & Lockman (1990), calculated using WebPIMMS. Column (4) Signal-to-noise ratio of the detected sources. Column (5) Count rate in the 0.5–2 keV band. Column (6) Count rate in the 2–8 keV band. Column (7) Photon index, where $N(E) \propto E^{-\Gamma_{\rm HR}}$, estimated from the hardness ratio (see the text). Column (8) Flux in the 0.5–2 keV band. Column (9) Flux in the 2–8 keV band. Column (10) Luminosity in the 0.5–2 keV band. Column (11) Luminosity in the 2–8 keV band. Column (12) Spectral index between 2500 Å and 2 keV, such that $\alpha_{\rm ox} = -0.3838 \log(f_{2500\text{Å}}/f_{\rm 2keV})$; see the text for details.

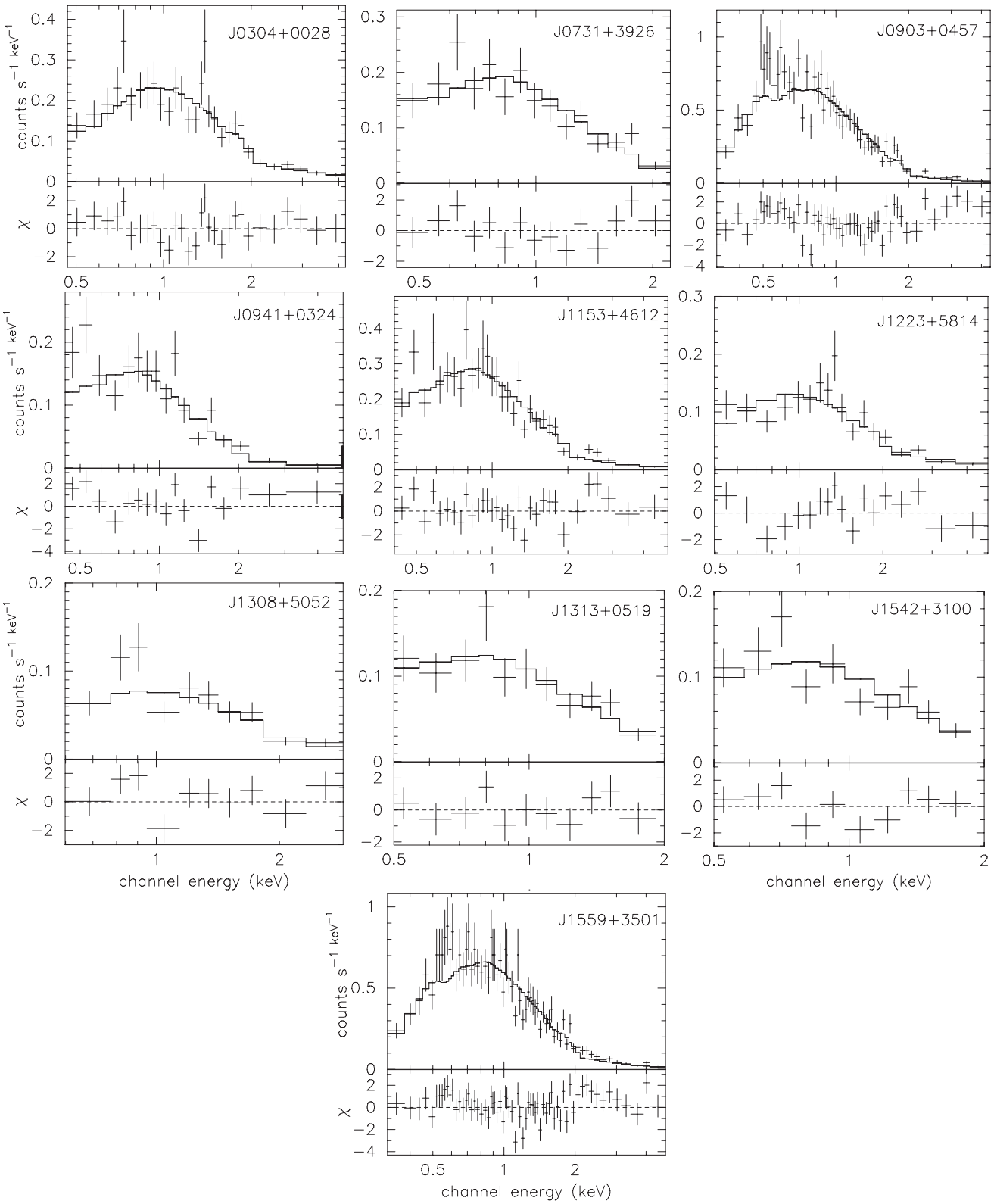

Figure 1. Spectral fits for the 10 sources with $\geqslant$ 200 counts. Each source is fitted with a single PL modified only by Galactic absorption. The bottom panel of each plot shows the residuals of the fit, expressed in terms of standard deviation χ with error bars of 1. Note that the energy range is adjusted in each individual plot due to different total source counts.

BH mass ($M_{\rm BH} \approx 10^5$–$10^{6.5}\,M_\odot$) and high Eddington ratios ($L_{\rm bol}/L_{\rm Edd} \approx 1$).[8] A major motivation of our analysis is to investigate whether these two characteristics impart any noticeable differences on the X-ray properties of AGNs. The X-ray observations presented here provide three basic tools to study the changes in accretion disk and corona with mass and Eddington ratio. First, we look at the X-ray spectrum itself. Second, we extract the X-ray variability properties with time.

[8] Although the bolometric correction remains uncertain, see below.

Table 2
Results of Spectral Fits

SDSS ID	Energy Range (keV)	Γ_s	Normalization (10^{-4} photon s^{-1} keV^{-1})	χ^2_ν	dof
(1)	(2)	(3)	(4)	(5)	(6)
J0304+0028	0.3–5	1.91 ± 0.08	5.35 ± 0.47	0.90	28
J0731+3926	0.3–3	2.71 ± 0.15	3.87 ± 0.41	0.98	13
J0903+0457	0.3–5	2.75 ± 0.06	11.75 ± 0.58	1.67	50
J0941+0324	0.3–5	2.52 ± 0.12	2.91 ± 0.32	1.58	20
J1153+4612	0.3–5	2.20 ± 0.08	5.39 ± 0.40	1.31	30
J1223+5814	0.3–5	1.54 ± 0.10	2.63 ± 0.32	1.42	16
J1308+5052	0.5–4	1.51 ± 0.20	1.64 ± 0.27	1.58	8
J1313+0519	0.3–3	2.50 ± 0.20	2.22 ± 0.29	0.74	9
J1542+3100	0.3–4	2.41 ± 0.18	2.17 ± 0.28	1.30	9
J1559+3501	0.3–5	2.29 ± 0.00	12.26 ± 0.56	1.29	65

Notes. Column (1) Abbreviated SDSS name. Column (2) Energy range used in the fit. Column (3) Photon index of power law, where $N(E) \propto E^{-\Gamma_s}$. Column (4) Normalization of the power law at 1 keV. Column (5) Reduced χ^2. Column (6) Degrees of freedom.

Third, the SED, and specifically the relative X-ray to UV flux, provides an important diagnostic of the accretion disk. As we will show, our measurements of the first two are not extensive enough to provide much new information. Therefore we focus mostly on the SED. First, we introduce the comparison samples that we use.

3.1. Comparison with Other Samples and Theoretical Models

To take full advantage of the dynamic range in BH mass and Eddington ratio afforded by our sample, we must utilize comparison samples from the literature. We compare our AGN sample with two other samples from recent literature: the "small clean" sample of (Wu et al. 2012a, hereafter W12), and the sample from Jin et al. (2012, hereafter J12). These two samples supplement ours in the parameters space of $L_{\rm bol}/L_{\rm Edd}$ and $M_{\rm BH}$. The W12 sample is composed of optically selected quasars from SDSS DR5, with simultaneous observations in the UV/optical and X-ray bands using *Swift*. These observations probe wavelengths closer to the big blue bump (BBB) than ground-based optical observations and simultaneously measure hard X-rays. Following W12, we limit the exposure time to be longer than 10 ks, resulting in a high X-ray detection rate of ∼85%. Based on the SED fitting, the authors determined the overall shape of the SED and subsequently derived the X-ray spectral slope, the bolometric luminosity $L_{\rm bol}$, and $L_{\rm bol}/L_{\rm Edd}$. $M_{\rm BH}$ in this sample ranges from $\sim 10^8$ to $10^9\ M_\odot$, and $L_{\rm bol}/L_{\rm Edd}$ ranges from $10^{-1.5}$ to $10^{0.5}$.

The J12 sample contains 51 unobscured type 1 AGNs, with $M_{\rm BH}$ spanning ∼1.5 dex around $10^8\ M_\odot$, and $\log L_{\rm bol}/L_{\rm Edd}$ about 2 dex centered at 0.3. These objects are X-ray/optically selected to have high-quality *XMM-Newton* and SDSS spectra in the literature. The sample is characterized by low reddening in the optical and low gas columns as implied by their X-ray spectra, so that the observed properties are likely to be intrinsic. The authors fit the data with an energetically self-consistent accretion disk model recently proposed by Done et al. (2012) to determine the overall shape of the SEDs and various properties of the sources. The Done et al. (2012) model contains three distinct spectral components, all powered by the energy released by a single accretion flow of constant mass accretion rate $\dot{M}$, onto a BH with mass $M_{\rm BH}$. The model assumes that the disk emission from outside a coronal radius $R_{\rm cor}$ thermalizes to a blackbody, with a color temperature correction. At radii smaller than $R_{\rm cor}$, the energy released from accretion is split between optically thick Comptonized disk emission, which forms the soft X-ray excess, and optically thin coronal emission above the disk, which forms the high-energy X-ray tail.

In addition to these two samples, we will also compare our targets with other NLS1s. The objects in our sample, with relatively narrow broad lines ($\rm FWHM_{H\alpha} < 2000\,km\,s^{-1}$), technically all qualify as NLS1s according to the line width criterion commonly used to define them, although given their mass cut our objects tend to occupy the low-mass end of the NLS1 class. The two groups share a number of other properties, including the propensity to have high Eddington ratios (GH07), weak radio emission (Greene et al. 2006), and low-mass and low-luminosity host galaxies (Greene et al. 2008; Jiang et al. 2011b), although some optical spectroscopic properties, such as the distribution of the strength of the Fe II and [O III] lines, are somewhat different (GH04; GH07).

3.2. X-Ray Spectra

The X-ray spectral index Γ is an important parameter that characterizes the disk-corona structure. Many papers have reported a correlation between Γ (usually measured at 2–10 keV) and the Eddington ratio (e.g., Laor et al. 1997; Shemmer et al. 2008; Risaliti et al. 2009). Theoretically, the interpretation is that as the UV flux from the disk increases, Compton cooling is more effective, leading to a steeper power-law slope (e.g., Pounds et al. 1995; Cao 2009). On the other hand, more recent studies of local active galaxies with lower luminosity and lower BH mass have not confirmed these relations, but rather observe a wide range of Γ values (Ai et al. 2011; Kamizasa et al. 2012). At lower $L_{\rm bol}/L_{\rm Edd}$, there is a suggestion that the X-ray spectral slope changes (Constantin et al. 2009) in analogy with that the spectral state changes from hard to soft seen when X-ray binaries go from a low to a high state (e.g., Meier 2001; Maccarone et al. 2003). We would like to investigate the distribution of Γ values in our sample, but unlike the aforementioned papers, we have not measured Γ directly. Instead, we have inferred it from the hardness ratio based on a limited spectral range.

We use disk models to test the correspondence between our measured Γ values and the intrinsic spectral shape. We generate mock AGN spectra using the Done et al. (2012) model described above (model optxagnf in XSPEC), which contains a hard power-law component characterized by an input Γ. We then "observe" these models using the same instrument response files as our targets, and recover $\Gamma_{\rm HR}$. We ask how $\Gamma_{\rm HR}$ compares with

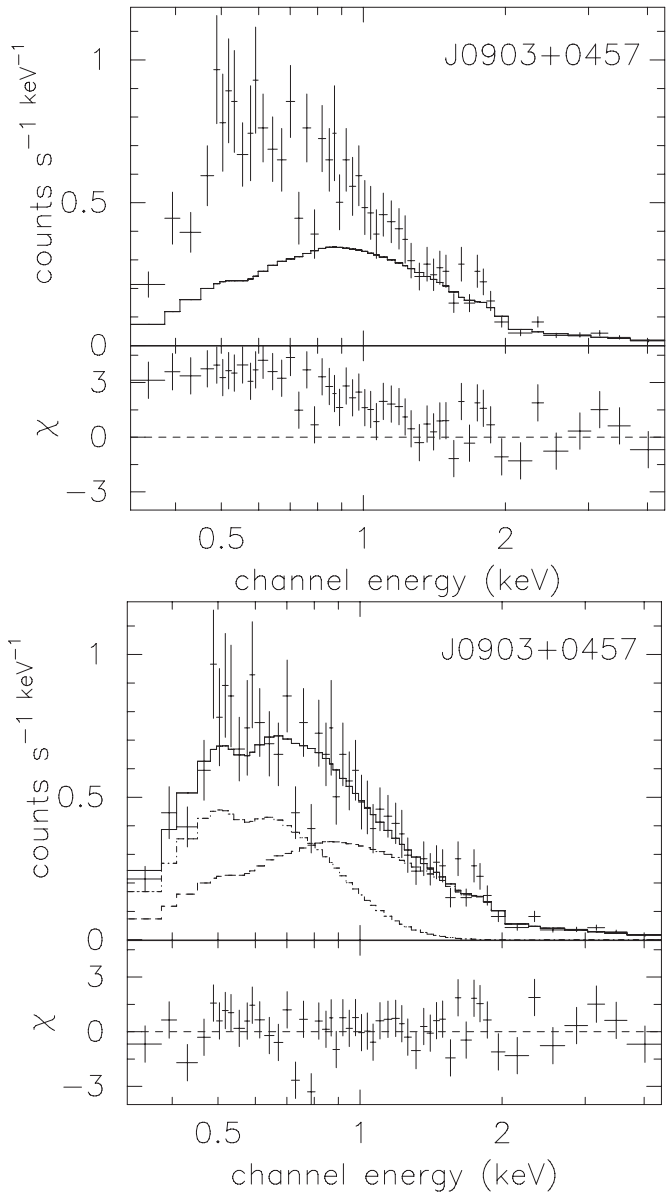

Figure 2. Multi-component fit of J0903+0457. (Left) A PL fit restricted to the energy range 1.5–5 keV; when extrapolated toward lower energies, a soft excess is clearly visible. (Right) A model consisting of the previous PL plus an additional `diskbb` component (with the solid curve showing the combination and the dashed curves showing the two individually) provides a reasonable fit to the entire spectrum. The bottom panel of each plot shows the residuals of the fit, expressed in terms of standard deviation χ with error bars of 1.

the intrinsic Γ. Unfortunately, we find that $\Gamma_{\rm HR}$ is not an accurate tracer of Γ. Specifically, for values of $\Gamma > 2$, $\Gamma_{\rm HR}$ is highly correlated with Γ. However, when $\Gamma < 2$ (flat), $\Gamma_{\rm HR}$ becomes steep again because of the soft X-ray excess. Our sensitivity to hard photons is too poor to return a high-fidelity measurement of Γ in the presence of complex, multi-component spectra. Therefore, we cannot directly compare our measurements with those based on *XMM-Newton* spectra that extend to much harder energies. We note that a similar effect may be present in higher redshift sources as well (e.g., W12). In this work we report our measurements of Γ, with the histogram shown in Figure 4, but avoid detailed comparison between our sample and others on Γ-related properties. $\Gamma_{\rm HR}$ in our sample ranges from ∼0.5–3, with a mean value of 2 and 1σ deviation of 0.5.

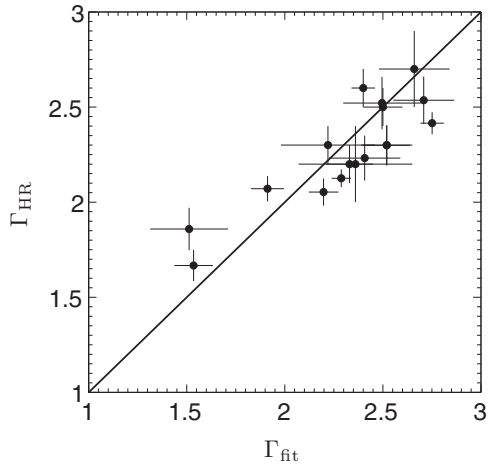

Figure 3. Comparison of the X-ray photon index $\Gamma_{\rm HR}$, calculated from the HR method, and $\Gamma_{\rm fit}$, which is derived directly from spectral fitting, for the 17 sources from the combined sample that have enough counts to allow spectral fitting. The solid diagonal line is the 1:1 relation. The two photon indices generally agree well within the range of Γ probed.

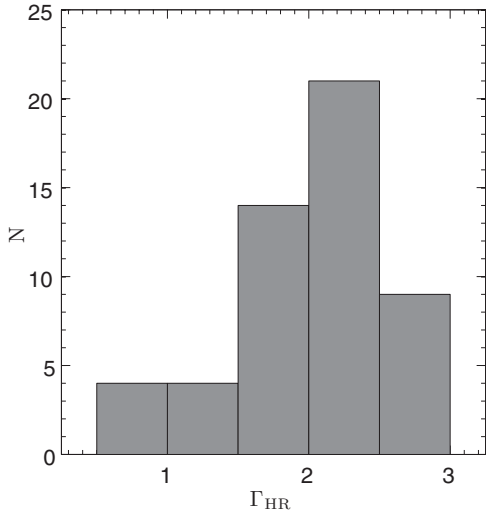

Figure 4. Distribution of $\Gamma_{\rm HR}$ for all *Chandra*-detected sources. Each bin is 0.5 in width in $\Gamma_{\rm HR}$.

Larger samples of NLS1s with deeper spectroscopy often exhibit complex features in their soft X-ray spectra. These include absorption edges due to O VII (0.74 keV) and O VIII (0.97 keV) and Fe K shell emission (Brandt et al. 1994; Leighly et al. 1997; Fiore et al. 1998; Turner et al. 1998; Nicastro et al. 1999), although their origin is not well understood (Ross & Fabian 2005). While we do not have enough sensitivity to detect any specific spectral features in this energy band, we do find, in agreement with Paper I, that most of our spectra show some evidence for spectral complexity around 1 keV.

4. THE RATIO OF OPTICAL/UV TO X-RAYS

We now consider the broader SEDs of the sample, and specifically the balance of energy coming out in the optical/UV emerging from the accretion disk as compared with the X-ray luminosity from the corona. We use the ratio of the optical-to-X-ray flux, $\alpha_{\rm ox}$, first introduced by Tananbaum et al. (1979). In general, there are three ways to interpret the range in $\alpha_{\rm ox}$:

1. In a standard disk, the balance of UV to X-ray photons is established via inverse-Compton scattering of UV photons

into a corona (e.g., Liang & Price 1977; Haardt & Maraschi 1993). Thus, changing the temperature of the disk, either by changing the BH mass or by changing the accretion rate, will lead to changes in the fraction of the disk energy that is reprocessed into the corona. Self-consistent magnetohydrodynamics simulations describing the fraction of energy emerging in the corona for stellar-mass BHs are in development now (e.g., Schnittman et al. 2012).

2. Another way to change α_{ox} is to change the structure of the disk entirely. If at high accretion rates, for instance, the disk structure changes from a standard α-disk to a slim disk (Abromowicz & Brown 1987; Abramowicz et al. 1988), then the disk may become very small and hot, and the fraction of energy in the disk may increase (e.g., Mineshige et al. 2000). Alternatively, the corona may disappear, leading to high $\dot{M}$ but intrinsically X-ray-weak sources (Leighly et al. 2007a, 2007b; Wu et al. 2012b). In X-ray binaries, the power-law emission often almost completely disappears in sources radiating above a few percent of Eddington (e.g., Remillard & McClintock 2006).
3. A third way to change α_{ox} is through absorption. Reddening will lower the UV luminosity and flatten the UV slope, while absorption in the X-rays will harden Γ and suppress the soft X-ray flux. However, as shown by, for example, Vasudevan et al. (2009), there is not always a direct connection between red quasars in the optical and X-ray-obscured systems. Thus, variations in absorption with time will add noise to intrinsic trends in α_{ox} (Gallo 2006), while trends between α_{ox} and UV luminosity may be partially attributable to uncorrected reddening (Vasudevan et al. 2009). Also, we note that different gas-to-dust ratios can cause different amounts of absorption between X-rays and optical, as has been explored in the context of gamma-ray bursts (e.g., Perley et al. 2009; Zafar et al. 2011).

Many papers have studied whether α_{ox} changes with either M_{BH} or L_{bol}/L_{Edd}. In this section, by extending the dynamic range in M_{BH} by an order of magnitude, we investigate the statistics of α_{ox} of our sample, and the correlation between α_{ox} and various quantities. Ultimately, we seek differences in the intrinsic SEDs of these active nuclei due to their mass or Eddington ratio, and what they tell us about disk structure.

4.1. α_{ox} and Correlations with Fundamental Parameters

We tabulate α_{ox} for our sample in Table 1. To be consistent with most authors in the current literature, we adopt the definition

$$\alpha_{ox} \equiv -0.3838 \log f_{2500}/f_{2keV}, \quad (1)$$

where $f_\nu \propto \nu^{\alpha_{ox}}$ is the specific flux. Note that this definition differs from the original one in Tananbaum et al. (1979) by a minus sign. Following Paper II, we use Hα measurements from GH07 to determine the AGN luminosity at 5100 Å (L_{5100}, Greene & Ho 2005),

$$L_{H\alpha} = 5.25 \times 10^{42} \left(\frac{L_{5100}}{10^{44}\ \mathrm{erg\ s^{-1}}} \right)^{1.157} \mathrm{erg\ s^{-1}}, \quad (2)$$

and then assume that the optical continuum follows the PL $f_\nu \propto \nu^{-0.44}$ (Vanden Berk et al. 2001; Greene & Ho 2007a) to calculate the monochromatic flux at 2500 Å (f_{2500}). We do not use the directly measured monochromatic flux at 5100 Å to avoid potential contamination by the galaxy starlight. Thus, we are less susceptible to reddening than in the case of a direct measurement

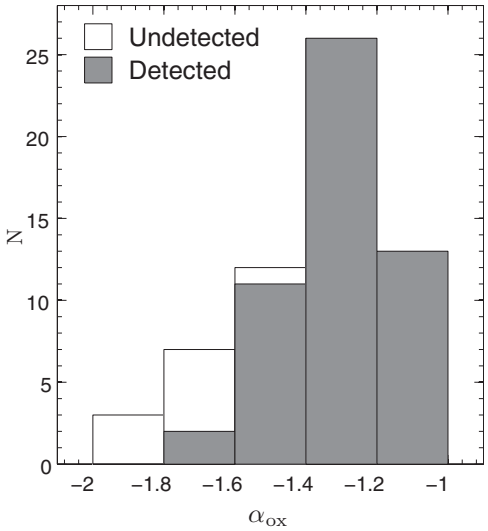

Figure 5. Distribution of α_{ox} for our sample; each bin is 0.2 in width in α_{ox}.

but depend on an assumed UV spectral slope. In cases where UV fluxes are available in the literature (see next paragraph) we find good consistency with our measurements, suggesting that our assumptions are valid. The X-ray monochromatic flux at 2 keV (f_{2keV}) is calculated from Γ_{HR} and f_s. We note that except for SDSS J0903+0457, which shows a prominent soft blackbody component in addition to the PL component, the monochromatic flux at 2 keV comes almost completely from the PL component.

Six objects from the GH04 sample were observed with *XMM-Newton* by Dewangan et al. (2008; see also Miniutti et al. 2009). Dewangan et al. (2008) took advantage of the Optical Monitor onboard *XMM-Newton* to record simultaneous optical/UV and X-ray fluxes, which enabled them to obtain more reliable measurements of α_{ox} for these objects. From comparison of α_{ox} between Paper II and Dewangan et al. (2008), we find a systematic offset of $\sim$0.1, with the *Chandra* values being slightly flatter (more X-ray luminous). We compare the values of L_{2500} from direct measurements using *XMM-Newton* (Miniutti et al. 2009) with our values derived from $L_{H\alpha}$ and find that the two agree well (although extinction may still be a factor in individual cases; Vasudevan et al. 2010). On the other hand, our *Chandra* X-ray luminosities are systematically higher than those derived from *XMM-Newton*, which accounts for the difference in α_{ox}. The level of difference, however, is small, and does not affect any of the conclusions below.

As in Paper II, we find that the ratio of X-rays to UV is higher in our sample of IMBHs than in AGNs with higher black hole mass. The values in our sample range from $\alpha_{ox} \approx -1.7$ to -1 (Figure 5; excluding upper limits), with an average of -1.33 and a standard deviation of 0.16, higher than $\langle\alpha_{ox}\rangle = -1.47 \pm 0.16$ for the W12 sample, and $\langle\alpha_{ox}\rangle = -1.56 \pm 0.22$ for the 87 Boroson & Green (1992) Palomar-Green (PG; Schmidt & Green 1983) QSOs with $z < 0.5$ and $10^7\ M_\odot \lesssim M_{BH} \lesssim 10^9\ M_\odot$ studied by Brandt et al. (2000; we converted their definition of α_{ox} to the conventions adopted in this paper). On the other hand, our values are closer to those measured for the J12 sample, $\langle\alpha_{ox}\rangle = -1.36 \pm 0.14$. In general, our α_{ox} values are flatter than those of SDSS-selected NLS1s (Figure 3 in Paper II), although both samples are drawn from the same parent sample, and are similar to those of the X-ray-selected NLS1s studied by Grupe et al. (2004, 2010). These flatter values of α_{ox} are expected from

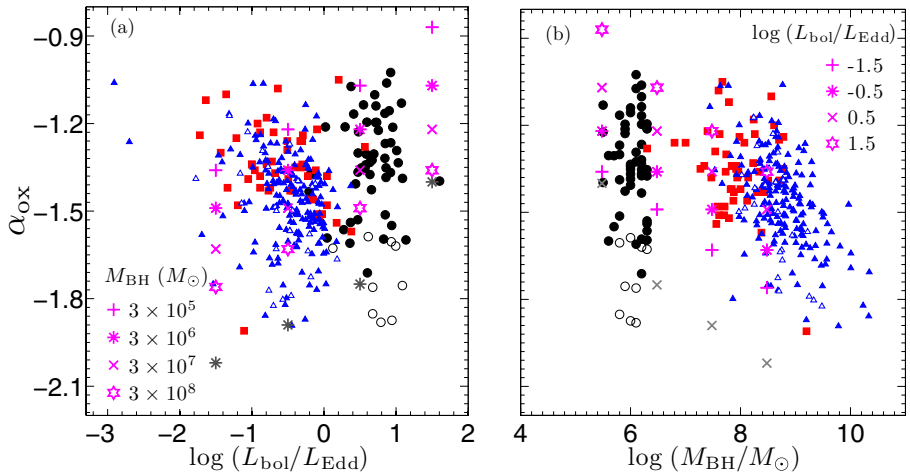

Figure 6. Dependence of α_{ox} on L_{bol}/L_{Edd} (a) and M_{BH} (b). The black circles are from our IMBH sample, the red squares are from the J12 sample, and the blue triangles are from W12. The open symbols in each sample, whenever relevant, indicate the non-detections. Done et al. (2012) models are indicated by +, ⋆, ×, and hexagrams. The magenta symbols assume $R_{cor} = 30r_g$, while the cyan symbols assume $R_{cor} = 8r_g$.
(A color version of this figure is available in the online journal.)

the well-known correlation between α_{ox} and monochromatic UV luminosity at 2500 Å (Avni & Tananbaum 1982; Bechtold et al. 2003; Strateva et al. 2005; Steffen et al. 2006). We note, however, that the α_{ox} values in our sample span a wide range. On average they statistically tend to lie *below* the best-fitting α_{ox}–l_{2500} relation of Steffen et al. (2006). We will return to the "X-ray-weak" sources in Section 5.

We turn to putative correlations between α_{ox} on the one hand and M_{BH} and L_{bol}/L_{Edd} on the other (Figure 6). L_{bol} is derived from the specific luminosity at 5100 Å ($L_{5100} = l_{5100}\nu_{5100}$). For consistency with the J12 sample, we use an M_{BH}-dependent bolometric correction factor. As the disk temperature increases for lower-mass BHs, less and less of the bolometric luminosity emerges in the optical and near-UV spectrum, leading to a mass-dependent bolometric correction. We fit a trend to the J12 data (their Table D1):

$$\log \frac{L_{bol}}{L_{5100}} = -0.54 \log M_{BH} + 5.43. \quad (3)$$

The bolometric correction factor used for the W12 sample (see also Richards et al. 2006) is consistent with the J12 trend in Equation (3) given the BH mass range of the W12 sample. The Eddington ratios that we derive here are approximately ∼1 dex higher than what we derive from canonical bolometric corrections (GH07), and these rather extreme values lead to super-Eddington accretion in our sources. However, since L_{bol}/L_{Edd} for both comparison samples is derived based on SED model fitting with similar bolometric correction factors, our approach is necessary in order to make the comparison consistent. In addition, as discussed in Section 1, we have some confidence in our black hole mass estimates on average based on the properties of their host galaxies despite the fact that they are derived through indirect methods. We also note that our conclusions would not change if we adopted our standard bolometric corrections, since we find no correlation between α_{ox} and L_{bol}/L_{Edd} in either case.

Consistent with Papers I and II, α_{ox} shows no clear dependence on L_{bol}/L_{Edd}. The lack of correlation has been seen by many authors recently, spanning a wide range in redshift, M_{BH}, and luminosity (Shemmer et al. 2008; Vasudevan et al. 2009; J12; W12). On the other hand, there is a hint of a trend between M_{BH} and α_{ox}. In particular, there is a dearth of objects with high values of M_{BH} and α_{ox}. Figure 6 nicely emphasizes the importance of our sample in extending the dynamic range of existing samples, particularly in M_{BH}. It is the extra decade in M_{BH} that highlights a weak trend between M_{BH} and α_{ox}.

To guide our interpretation, we also include theoretical predictions from the Done et al. (2012) model. We show tracks in M_{BH} and L_{bol}/L_{Edd}, while leaving the other parameters fixed to default parameters following Jin et al. (2012): $kT_e = 0.2$ keV (electron temperature for the soft Comptonization component), $\tau = 10$ (optical depth of the soft Comptonization component), $\Gamma = 2$ (spectral index of the hard Comptonization component), and $f_{pl} = 0.1$ (fraction of the power below R_{cor} that is emitted in the hard Comptonization component). After experimenting with different choices of these additional parameters, we find that although the exact value of α_{ox} at a given M_{BH} and L_{bol}/L_{Edd} is affected by their specific values, the predicted trends between α_{ox} and M_{BH} or L_{bol}/L_{Edd} are robust. There is also a long tail toward X-ray weakness in our sample. In Section 5, we will discuss whether these are absorbed or intrinsically weak sources. For now, we simply highlight the gray symbols in Figure 6, which have $R_{cor} = 8R_g$ rather than $R_{cor} = 30R_g$ but otherwise are constructed with the same parameters. Going from $R_{cor} = 30R_g$ to $R_{cor} = 8R_g$ the coronal component of the disk shrinks, so that the Comptonization and the X-ray component of the disk spectrum become weaker, and the disk emission is more dominated by the (color-temperature corrected) blackbody component.

In the Done et al. (2012) models, changes in α_{ox} are driven predominantly by changes in the accretion disk temperature, which preferentially move the UV luminosity up and down as the peak BBB temperature approaches and recedes from 2500 Å. Using α_{ox} we are not very sensitive to intrinsic changes in the X-ray SED with M_{BH} and L_{bol}/L_{Edd} (Vasudevan et al. 2009; Jin et al. 2012), but we can detect changes in the BBB temperature. At fixed L_{bol}/L_{Edd}, the BBB temperature decreases systematically with M_{BH}, leading to higher (i.e., more positive) values of α_{ox} at lower M_{BH}. The trend is highlighted clearly in the models but is apparent in the data as well, with the mean α_{ox} dropping from −1.33 at $M_{BH} \approx 10^6$–$10^7\,M_\odot$, to −1.35 at $M_{BH} \approx 10^7$–$10^8\,M_\odot$, −1.42 at $M_{BH} \approx 10^8$–$10^8\,M_\odot$, and

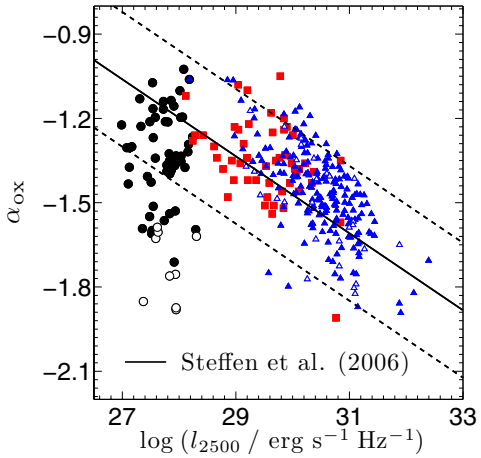

Figure 7. Dependence of α_{ox} on the monochromatic luminosity at 2500 Å (l_{2500}). The black circles are from our IMBH sample, the red squares are from the J12 sample, and the blue triangles are from W12. The open symbols in each sample, whenever relevant, indicate the non-detections. The solid line is the best-fit relation from Steffen et al. (2006), and the dashed lines indicate the 1σ deviations.

(A color version of this figure is available in the online journal.)

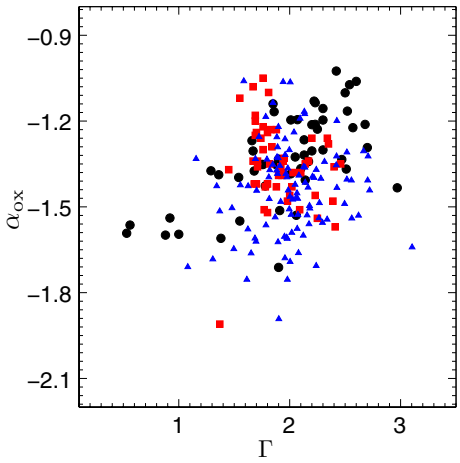

Figure 8. Dependence of α_{ox} on the X-ray photon index. The black circles are from our IMBH sample, the red squares are from the J12 sample, and the blue triangles are from W12.

(A color version of this figure is available in the online journal.)

-1.56 at $M_{BH} \approx 10^9$–$10^{10}\,M_\odot$. The scatter is obviously very large, presumably due to a spread in luminosity, absorption, and corona-properties at fixed M_{BH}. In Figure 7, we show the correlation between α_{ox} and l_{2500}. The BH mass is calculated using the same luminosity that is the independent variable in Figure 7. In both cases the correlation is weak—the linear correlation coefficient for $\alpha_{ox}-\log M_{BH}$ is 0.41, while for $\alpha_{ox}-\log l_{2500}$ it is 0.45. However, we suggest that the correlation between M_{BH} and α_{ox} may be the more fundamental one, arising simply from changes in the accretion disk temperature. We suggest that the α_{ox}–l_{2500} correlation appears so strong because there is a narrow range in L_{bol}/L_{Edd} at a given M_{BH}.

5. X-RAY-WEAK SOURCES

As we have seen in the above section, our sample spans a wide range in α_{ox} but there is a clear excess of points that fall systematically below the low-luminosity extrapolation of the α_{ox}–l_{2500} relation of Steffen et al. (2006) defined by more luminous sources. In other words, some IMBHs appear to be suppressed in X-rays (relative to the UV). Heavy obscuration provides a simple explanation for the X-ray-weak sources. Indeed, in Figure 8 we see a trend toward flat Γ values in the X-ray-weak sources, implicating absorption.

However, not all the sources follow this trend. There are a few objects in Figure 8 that have typical sample-averaged Γ values ($\sim$2) but low α_{ox} values. They raise the intriguing possibility that some of these sources are intrinsically X-ray-weak. In Figure 9(a), we show the relation between 2 keV and UV luminosity in a slightly different way. For reference we have added the sample of $z < 0.5$ PG QSOs from Brandt et al. (2000; light blue diamonds), highlighting in magenta hexagrams the subset of objects that they dub X-ray-weak quasars. These comprise broad absorption-line quasars, and deep X-ray observations confirm that their X-ray weakness is caused by absorption (e.g., Gallagher et al. 2001; Brinkmann et al. 2004; Schartel et al. 2005; Ballo et al. 2008; Gallo et al. 2011; Stern & Laor 2012). A minority, however, appear to be genuinely X-ray-weak (e.g., Risaliti et al. 2001; Sabra & Hamann 2001; Leighly et al. 2007a; Miniutti et al. 2009; Ballo et al. 2011), and this unusual spectral departure has been suggested to be a possible signature of accretion systems with high Eddington ratios. PHL 1811 is the prototype: Not only are its X-rays unabsorbed, but they vary on a short time scale, indicating a compact size. Such objects are quite rare among optically selected samples of QSOs, comprising less than 2% of QSOs in SDSS (Gibson et al. 2008).

In the absence of UV spectroscopy or X-ray variability information, it is difficult to say for certain whether any of our sources are intrinsically X-ray-weak. In view of the bias toward high accretion rates in IMBHs, intrinsic weakness is an attractive possibility to account for the large fraction of X-ray-weak sources in our sample. As mentioned before, type 1 IMBHs, as a class, show little direct evidence for additional absorption above the Galactic value. A few of the X-ray-weak sources do have exceptionally hard X-ray spectra, with $\Gamma \approx 1$, but the majority, in fact, have photon indices that span the same range as observed for the X-ray "normal" sources ($\Gamma_s \approx 1.5$–3; Figure 7). Also, notably, Brandt et al.'s X-ray-weak PG QSOs form a disjoint group significantly offset from the main population in Figure 9(a) (average UV/X-ray ratio lower by a factor $\sim$60), whereas, by contrast, our X-ray-weak sources seem to join more or less smoothly in a continuous sequence with the "normal" sources (average UV/X-ray ratio lower by a factor $\sim$5).

A similar perspective comes from comparing the X-ray luminosity with some measure of optical line emission, as the two are strongly correlated in unobscured AGNs (e.g., Elvis et al. 1984; Ward et al. 1988; Mulchaey et al. 1994; Terashima et al. 2000; Ho et al. 2001; Heckman et al. 2005). Heavily obscured AGNs, such as Compton-thick systems, fall off the correlation in being underluminous in X-rays for a given optical line luminosity (e.g., Bassani et al. 1999). The correlation between 2 and 10 keV luminosity with [O III] λ5007 luminosity is shown in Figure 9(b), where, for comparison, we include the best-fitting relation from a sample of low-luminosity Seyferts in Panessa et al. (2006). The X-ray-weak IMBHs do tend to lie systematically below the relation defined by the higher luminosity sources, suggesting that absorption is likely an explanation for many of the sources, but perhaps not all.

In principle, infrared data could also serve as a proxy for the bolometric luminosity of the system, to indicate whether the UV-weak sources are absorbed or intrinsically weak. We examine the

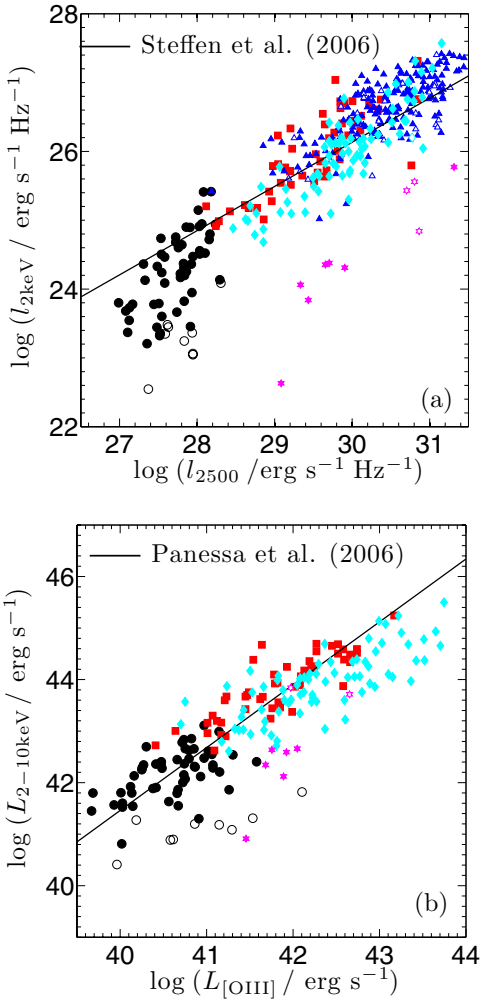

Figure 9. l_{2keV} as a function of l_{2500} (a), and $L_{2-10keV}$ as a function of $L_{[O III]}$ (b). The solid lines are the best-fit relations from past literature. The black circles are from our IMBH sample, the red squares are from the J12 sample, and the blue triangles are from W12. For the IMBHs, $L_{2-10keV}$ is calculated from L_{2-8keV} and Γ_{HR}. We also include the PG QSOs from Brandt et al. (2000; light blue diamonds; soft X-ray-weak objects shown in magenta hexagrams), using values of $L_{2-10keV}$ estimated from L_{5100}, α_{ox}, an assumed optical–UV spectrum $f_\nu \propto \nu^{-0.44}$ (Vanden Berk et al. 2001), and $\Gamma_h = 1.9$ (Piconcelli et al. 2005); $L_{[O III]}$ was derived from the [O III] equivalent widths of Boroson & Green (1992) and the optical spectrophotometry of Neugebauer et al. (1987). Open symbols indicate the X-ray non-detections.

(A color version of this figure is available in the online journal.)

IR luminosities of our sample in the *Wide-field Infrared Survey Explorer* (*WISE*) all-sky catalog.[9] All of our objects except three are detected in *WISE*. However, the distribution of their W1–W2 colors (mean = 0.63, σ = 0.27) suggests that the photometry is dominated by the light from the host galaxies in most cases (Assef et al. 2012). This is consistent with the beam size of the *WISE* observations (6″–12″ at various bands). Without detailed SED decomposition, it is not possible to determine the AGN luminosities from the *WISE* data alone. We need to await higher resolution data.

At the moment, the true nature of the X-ray-weak sources is unclear. We suggest two future observations that could test whether the observed X-ray weakness is truly intrinsic:

1. X-ray observations with enough counts and energy resolution to allow detailed spectral fitting to determine whether there is evidence for intrinsic absorption.
2. High-resolution IR observations to check whether the X-ray photons have been absorbed and reprocessed as IR emission by dust.

6. SUMMARY

We carry out a study of the X-ray properties of 49 IMBHs in active galaxies selected from the GH07 sample using *Chandra* data. We detect 42 out of 49 objects at the SDSS position. The main results are consistent with Greene & Ho (2007a) and Desroches et al. (2009). We perform spectral analysis of 10 objects with sufficient counts, and all of them are consistent with a Galactic absorbed power-law model. Spectral fitting with intrinsic absorption and an additional disk blackbody component generally produce a poor result, yielding essentially zero intrinsic column density as well as unphysical T_{in}. We conclude that there is no significant sign of intrinsic absorption or a disk blackbody component in the bright sources. For two objects with enough counts in the hard X-ray band, we fit the spectra using an absorbed power-law model using data $\geqslant$1.5 keV, then extrapolate it to the whole energy range. SDSS J1559+3501 shows good agreement between the extrapolation and the spectra at lower energy, while SDSS J0903+0457 shows a prominent soft excess. We conclude that with enough counts, both situations are possible in the low-mass regime.

The Γ values that we measure for the IMBH sample occupy the same range (0.5–3) as their more luminous counterparts. However, given the limited spectral range of our 2 ks observations, we caution against detailed comparisons between our inferred slopes and those based on detailed spectroscopy with energy sensitivity at $\gtrsim$ 10 keV. Exploring the true range in Γ requires deeper spectroscopy.

Our sample contains significantly flatter values of α_{ox} than in more luminous PG QSOs (Brandt et al. 2000) and SDSS-selected NLS1s (Paper II). Our values of α_{ox} generally agree with the low-luminosity extrapolation of the well-known α_{ox}–l_{2500} correlation, but, at a given UV luminosity, there is a tendency for IMBHs to be more X-ray-weak. While absorption may be partly responsible for this trend, we suggest the intriguing possibility that some of the objects may be intrinsically X-ray-weak, as previously suggested for AGNs with high L_{bol}/L_{Edd}. Deeper X-ray follow-up of the X-ray-weak sources would determine whether some significant fraction of our sample is actually in a mode of accretion with little to no X-ray corona.

While α_{ox} shows no correlation with L_{bol}/L_{Edd}, we do find a mild correlation between α_{ox} and M_{BH}, in just the sense expected by disk models. As M_{BH} drops, the disk temperature increases, and the sources grow fainter in the near-UV, thus increasing the level of X-rays relative to the UV flux. Indeed, this correlation between α_{ox} and M_{BH} may drive the well-known correlation between l_{2500} and α_{ox}. Considering that extinction, variations in the corona, and uncertainties in the M_{BH} measurements all wash out this trend, the large dynamic range in M_{BH} afforded by our sample is essential to detect any correlation at all.

We thank Xiao-Bo Dong and Jesper Rasmussen for useful discussions, Louis-Benoit Desroches for providing part of the comparison data, and Craig Gordon from the XSPEC online help team for technical support. The authors are also grateful

[9] http://irsa.ipac.caltech.edu/applications/Gator

to the anonymous referee who helped improve the manuscript. This work was funded through SAO grant 11700259.

REFERENCES

Abromowicz, M., & Brown, M. 1987, Astrophys. Lett., 25, 205
Abramowicz, M. A., Czerny, B., Lasota, J. P., & Szuszkiewicz, E. 1988, ApJ, 332, 646
Ai, Y. L., Yuan, W., Zhou, H. Y., Wang, T. G., & Zhang, S. H. 2011, ApJ, 727, 31
Arnaud, K. A. 1996, in ASP Conf. Ser. 101, Astronomical Data Analysis Software and Systems V, ed. G. H. Jacoby & J. Barnes (San Francisco, CA: ASP), 17
Assef, R. J., Stern, D., Kochanek, C. S., et al. 2012, arXiv:1209.6055
Avni, Y., & Tananbaum, H. 1982, ApJ, 262, L17
Ballo, L., Giustini, M., Schartel, N., et al. 2008, A&A, 483, 137
Ballo, L., Piconcelli, E., Vignali, C., & Schartel, N. 2011, MNRAS, 415, 2600
Barth, A. J., Greene, J. E., & Ho, L. C. 2005, ApJ, 619, L151
Bassani, L., Dadina, M., Maiolino, R., et al. 1999, ApJS, 121, 473
Bechtold, J., Siemiginowska, A., Shields, J., et al. 2003, ApJ, 588, 119
Bentz, M. C., Walsh, J. L., Barth, A. J., et al. 2009, ApJ, 705, 199
Boroson, T. A., & Green, R. F. 1992, ApJS, 80, 109
Brandt, W. N., Fabian, A. C., Nandra, K., Reynolds, C. S., & Brinkmann, W. 1994, MNRAS, 271, 958
Brandt, W. N., Laor, A., & Wills, B. J. 2000, ApJ, 528, 637
Brinkmann, W., Arévalo, P., Gliozzi, M., & Ferrero, E. 2004, A&A, 415, 959
Cantrell, A. G., Bailyn, C. D., Orosz, J. A., et al. 2010, ApJ, 710, 1127
Cao, X. 2009, MNRAS, 394, 207
Constantin, A., Green, P., Aldcroft, T., et al. 2009, ApJ, 705, 1336
Crummy, J., Fabian, A. C., Gallo, L., & Ross, R. R. 2006, MNRAS, 365, 1067
Desroches, L.-B., Greene, J. E., & Ho, L. C. 2009, ApJ, 698, 1515 (Paper II)
Dewangan, G. C., Mathur, S., Griffiths, R. E., & Rao, A. R. 2008, ApJ, 689, 762
Dickey, J. M., & Lockman, F. J. 1990, ARA&A, 28, 215
Done, C., Davis, S. W., Jin, C., Blaes, O., & Ward, M. 2012, MNRAS, 420, 1848
Done, C., & Nayakshin, S. 2007, MNRAS, 377, L59
Dong, X.-B., Ho, L. C., Yuan, W., et al. 2012, ApJ, 755, 167
Elvis, M., Soltan, A., & Keel, W. C. 1984, ApJ, 283, 479
Elvis, M., Wilkes, B. J., McDowell, J. C., et al. 1994, ApJS, 95, 1
Fender, R. P., Homan, J., & Belloni, T. M. 2009, MNRAS, 396, 1370
Fiore, F., Matt, G., Cappi, M., et al. 1998, MNRAS, 298, 103
Gallagher, S. C., Brandt, W. N., Laor, A., et al. 2001, ApJ, 546, 795
Gallagher, S. C., Richards, G. T., Hall, P. B., et al. 2005, AJ, 129, 567
Gallo, E., Treu, T., Jacob, J., et al. 2008, ApJ, 680, 154
Gallo, L. C. 2006, MNRAS, 368, 479
Gallo, L. C., Grupe, D., Schartel, N., et al. 2011, MNRAS, 412, 161
Garmire, G. P., Bautz, M. W., Ford, P. G., Nousek, J. A., & Ricker, G. R., Jr. 2003, Proc. SPIE, 4851, 28
Gibson, R. R., Brandt, W. N., & Schneider, D. P. 2008, ApJ, 685, 773
Greene, J. E., & Ho, L. C. 2004, ApJ, 610, 722 (GH04)
Greene, J. E., & Ho, L. C. 2005, ApJ, 630, 122
Greene, J. E., & Ho, L. C. 2007a, ApJ, 656, 84 (Paper I)
Greene, J. E., & Ho, L. C. 2007b, ApJ, 670, 92 (GH07)
Greene, J. E., Ho, L. C., & Barth, A. J. 2008, ApJ, 688, 159
Greene, J. E., Ho, L. C., & Ulvestad, J. S. 2006, ApJ, 636, 56
Greene, J. E., Peng, C. Y., Kim, M., et al. 2010, ApJ, 721, 26
Grupe, D., Komossa, S., Leighly, K. M., & Page, K. L. 2010, ApJS, 187, 64
Grupe, D., Wills, B. J., Leighly, K. M., & Meusinger, H. 2004, AJ, 127, 156
Haardt, F., & Maraschi, L. 1993, ApJ, 413, 507
Heckman, T. M., Ptak, A., Hornschemeier, A., & Kauffmann, G. 2005, ApJ, 634, 161
Ho, L. C. 1999, ApJ, 516, 672
Ho, L. C., Feigelson, E. D., Townsley, L. K., et al. 2001, ApJ, 549, L51
Hu, J. 2008, MNRAS, 386, 2242
Jiang, Y.-F., Greene, J. E., & Ho, L. C. 2011a, ApJ, 737, L45
Jiang, Y.-F., Greene, J. E., Ho, L. C., Xiao, T., & Barth, A. J. 2011b, ApJ, 742, 68
Jin, C., Ward, M., & Done, C. 2012, MNRAS, in press (arXiv:1205.1846) (J12)
Kajava, J. J. E., & Poutanen, J. 2009, MNRAS, 398, 1450
Kamizasa, N., Terashima, Y., & Awaki, H. 2012, ApJ, 751, 39
Kaspi, S., Maoz, D., Netzer, H., et al. 2005, ApJ, 629, 61
Kormendy, J., & Bender, R. 2011, Nature, 469, 377
Krolik, J. H. 2001, ApJ, 551, 72
Laor, A., Fiore, F., Elvis, M., Wilkes, B. J., & McDowell, J. C. 1997, ApJ, 477, 93
Leighly, K. M. 1999, ApJS, 125, 317
Leighly, K. M., Halpern, J. P., Jenkins, E. B., et al. 2007a, ApJ, 663, 103
Leighly, K. M., Halpern, J. P., Jenkins, E. B., & Casebeer, D. 2007b, ApJS, 173, 1
Leighly, K. M., Kay, L. E., Wills, B. J., Wills, D., & Grupe, D. 1997, ApJ, 489, L137
Liang, E. P. T., & Price, R. H. 1977, ApJ, 218, 247
Ludwig, R. R., Greene, J. E., Barth, A. J., & Ho, L. C. 2012, ApJ, 756, 51
Maccarone, T. J., Gallo, E., & Fender, R. 2003, MNRAS, 345, L19
Meier, D. L. 2001, ApJ, 548, L9
Mineshige, S., Kawaguchi, T., Takeuchi, M., & Hayashida, K. 2000, PASJ, 52, 499
Miniutti, G., Ponti, G., Greene, J. E., et al. 2009, MNRAS, 394, 443
Mulchaey, J. S., Koratkar, A., Ward, M. J., et al. 1994, ApJ, 436, 586
Netzer, H. 1990, in Active Galactic Nuclei (Saas-Fee Advanced Course 20), ed. R. D. Blandford, H. Netzer, & L. Woltjer (Berlin: Springer-Verlag), 57
Neugebauer, G., Green, R. F., Matthews, K., et al. 1987, ApJS, 63, 615
Nicastro, F., Fiore, F., & Matt, G. 1999, ApJ, 517, 108
Panessa, F., Bassani, L., Cappi, M., et al. 2006, A&A, 455, 173
Perley, D. A., Cenko, S. B., Bloom, J. S., et al. 2009, AJ, 138, 1690
Piconcelli, E., Jimenez-Bailón, E., Guainazzi, M., et al. 2005, A&A, 432, 15
Porquet, D., Reeves, J. N., O'Brien, P., & Brinkmann, W. 2004, A&A, 422, 85
Pounds, K. A., Done, C., & Osborne, J. P. 1995, MNRAS, 277, L5
Rafter, S. E., Kaspi, S., Behar, E., Kollatschny, W., & Zetzl, M. 2011, ApJ, 741, 66
Remillard, R. A., & McClintock, J. E. 2006, ARA&A, 44, 49
Richards, G. T., Lacy, M., Storrie-Lombardi, L. J., et al. 2006, ApJS, 166, 470
Risaliti, G., Marconi, A., Maiolino, R., Salvati, M., & Severgnini, P. 2001, A&A, 371, 37
Risaliti, G., Young, M., & Elvis, M. 2009, ApJ, 700, L6
Ross, R. R., & Fabian, A. C. 2005, MNRAS, 358, 211
Sabra, B. M., & Hamann, F. 2001, ApJ, 563, 555
Schartel, N., Rodríguez-Pascual, P. M., Santos-Lleó, M., et al. 2005, A&A, 433, 455
Schmidt, M., & Green, R. F. 1983, ApJ, 269, 352
Schnittman, J. D., Krolik, J. H., & Noble, S. C. 2012, ApJ, in press (arXiv:1207.2693)
Shemmer, O., Brandt, W. N., Netzer, H., Maiolino, R., & Kaspi, S. 2008, ApJ, 682, 81
Shields, G. A. 1978, Nature, 272, 706
Spergel, D. N., Verde, L., Peiris, H. V., et al. 2003, ApJS, 148, 175
Steffen, A. T., Strateva, I., Brandt, W. N., et al. 2006, AJ, 131, 2826
Stern, J., & Laor, A. 2012, MNRAS, 423, 600
Strateva, I. V., Brandt, W. N., Schneider, D. P., Vanden Berk, D. G., & Vignali, C. 2005, AJ, 130, 387
Straub, O., Bursa, M., SaĎowski, A., et al. 2011, A&A, 533, A67
Tananbaum, H., Avni, Y., Branduardi, G., et al. 1979, ApJ, 234, L9
Terashima, Y., Ho, L. C., Ptak, A. F., et al. 2000, ApJ, 533, 729
Thornton, C. E., Barth, A. J., Ho, L. C., & Greene, J. E. 2009, ApJ, 705, 1196
Trichas, M., Green, P. J., Silverman, J. D., et al. 2012, ApJS, 200, 17
Turner, T. J., George, I. M., & Nandra, K. 1998, ApJ, 508, 648
Vanden Berk, D. E., Richards, G. T., Bauer, A., et al. 2001, AJ, 122, 549
Vasudevan, R. V., Mushotzky, R. F., Winter, L. M., & Fabian, A. C. 2009, MNRAS, 399, 1553
Vasudevan, R. V., Fabian, A. C., Gandhi, P., Winter, L. M., & Mushotzky, R. F. 2010, MNRAS, 402, 1081
Wang, Q. D., Yao, Y., Fukui, W., Zhang, S. N., & Williams, R. 2004, ApJ, 609, 113
Ward, M. J., Done, C., Fabian, A. C., Tennant, A. F., & Shafer, R. A. 1988, ApJ, 324, 767
Weisskopf, M. C., O'Dell, S. L., & van Speybroeck, L. P. 1996, Proc. SPIE, 2805, 2
Wu, J., Brandt, W. N., Anderson, S. F., et al. 2012b, ApJ, 747, 10
Wu, J., Vanden Berk, D., Grupe, D., et al. 2012a, ApJS, 201, 10 (W12)
Xiao, T., Barth, A. J., Greene, J. E., et al. 2011, ApJ, 739, 28
York, D. G., Adelman, J., Anderson, J. E., Jr., et al. 2000, AJ, 120, 1579
Zafar, T., Watson, D., Fynbo, J. P. U., et al. 2011, A&A, 532, A143